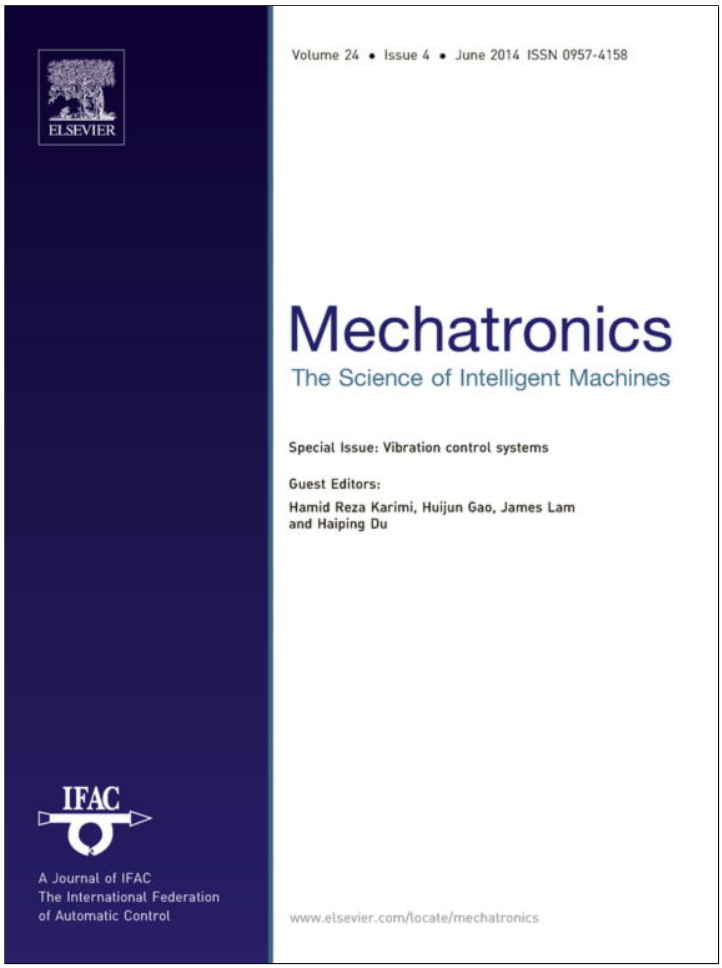

Mechatronics 24 (2014) 367–375

Contents lists available at SciVerse ScienceDirect

Mechatronics

journal homepage: www.elsevier.com/locate/mechatronics

Integral resonant damping for high-bandwidth control of piezoceramic stack actuators with asymmetric hysteresis nonlinearity

Guo-Ying Gu [a], Li-Min Zhu [a,*], Chun-Yi Su [b]

[a] State Key Laboratory of Mechanical System and Vibration, School of Mechanical Engineering, Shanghai Jiao Tong University, Shanghai 200240, China
[b] Department of Mechanical and Industrial Engineering, Concordia University, Montreal, Quebec H3G 1M8, Canada

ARTICLE INFO

Article history:
Available online 9 July 2013

Keywords:
Piezoceramic stack actuator
Integral resonant control
High-bandwidth control
Asymmetric hysteresis compensation

ABSTRACT

This paper presents a novel control scheme for high-bandwidth control of piezoceramic stack actuators (PSAs). For this purpose, we first characterize and compensate for the asymmetric hysteresis nonlinearity of the PSA. A linear integral resonant controller is then designed as a means for damping the resonant modes of the dynamic system with the hysteresis compensation. Finally, a tracking controller and feedforward input are developed to minimize the tracking errors and improve the closed-loop tracking bandwidth. To verify the effectiveness and efficiency of the proposed control scheme, a PSA-actuated positioning platform is built and comparative experiments are conducted. Experimental results demonstrate that the proposed controller achieves robust broadband nanopositioning of the PSA by improving the tracking bandwidth from 22 Hz (with an integral controller) to 657 Hz.

1. Introduction

Along with the rapid development of nanoscience and nanotechnology, nanopositioning stages are widely applied in many precision manufacturing equipments such as scanning probe microscopes (SPMs) [1,2] and diamond turning machines [3]. For instance, in SPMs, a nanopositioning stage is utilized to scan the probe over a sample surface with the nanometer or sub-nanometer positioning resolution and to control the interaction between the probe and the sample surface. Besides high-precision positioning, high-bandwidth operation of the stage is imperative when imaging the sample with a fast time-varying nature in order to avoid distortions.

A pivotal component of nanopositioning stages is a piezoceramic actuator due to its excellent advantages of high displacement resolution, fast response time and high stiffness [1,4]. However, the piezoceramic actuators have two main drawbacks limiting the accuracy and speed of the nanopositioning stages: (i) inherent hysteresis nonlinearity in the piezoceramic material [4,5] and (ii) low damped resonant modes due to the mechanical dynamics [6,7].

Hysteresis nonlinearity in the piezoceramic materials is one of the main problems degrading the positioning accuracy. In nanopositioning stages actuated by piezoceramic actuators, the existence of the hysteresis nonlinearity can produce positioning error up to 15% of the moving range at operating frequencies well below the first resonance mode of the piezo-actuated stage [8]. In worst case, it may cause the oscillation, or even instability of the control systems [4]. To remedy the hysteresis, many efforts have been made in the literature. The most common approach is to construct a model that can accurately describe the hysteresis nonlinearity and then preshape the input voltage based on the inverse of the model [9–13]. Rather than constructing the inverse hysteresis model, some attempts have been made to apply the feedback control approaches [14–16] to mitigate the hysteresis nonlinearity. As an alternative, charge actuation [17] of piezoceramic actuators has shown to be an effective method significantly reducing hysteresis nonlinearity compared with generally used voltage actuation. However, the charge amplifier has not been widely adopted due to its implementation complexity and cost.

Resonant modes are the major issue hindering the operation speed of the piezo-actuated nanopositioning stages, which restricts operating frequencies to less than 1/10–1/100th of the first resonance frequency of the stages to avoid the positioning problem at high operating speeds [18]. Although one may build a sufficiently stiff and small piezo-actuated stage to increase the operation speed, its maximum travel range is limited to a few microns. Even in this case, the tracking bandwidth is still limited by the resonant modes of the actuators [19]. Therefore, it requires development of control techniques to suppress the vibration effect. To address this issue, several strategies have been developed in the literature, including the input-shaping technique [20,21], the notch filter [6,22], and the inversion-based approach [23]. However, the solutions using these techniques are sensitive to variations of the

* Corresponding author. Tel.: +86 2134206545.
E-mail addresses: guguoying@sjtu.edu.cn (G.-Y. Gu), zhulm@sjtu.edu.cn (L.-M. Zhu), cysu@alcor.concordia.ca (C.-Y. Su).

0957-4158/$ - see front matter © 2013 Elsevier Ltd. All rights reserved.
http://dx.doi.org/10.1016/j.mechatronics.2013.06.001

resonant mode parameters in the system model [24,25]. As an alternative, feedback control is introduced to suppress the resonant vibrations, such as positive position feedback control [26], resonant control [27] and integral resonant control (IRC) [28]. Recently, the IRC strategy is demonstrated as a simple means for damping the vibrations, which has been successfully applied to piezoceramic tube actuators for fast nanoscale positioning [25]. However, the charge control is used in these applications. The use of IRC strategy for piezoceramic stack actuators driven by voltage control is still missing.

1.1. Contribution of this paper

The contribution of this paper is to propose a combined control scheme for high-bandwidth control of piezoceramic stack actuators (PSAs). The control objective is achieved by the following steps: (1) an inverse hysteresis compensator is designed to mitigate the asymmetric hysteresis nonlinearity using a modified Prandtl-Ishlinskii (MPI) model; (2) the IRC strategy is introduced as a means for damping the dynamic system with the inverse hysteresis compensation; (3) an integral tracking controller is developed to minimize tracking errors of the desired position y_d and the actual position y; (4) a feedforward input with the inverse dc gain of the system is utilized to further improve the tracking bandwidth of the closed-loop system; and (5) comparative experiments on a PSA-actuated stage are conducted in real time to verify the effectiveness of the proposed control scheme.

1.2. Outline

The remainder of this paper is organized as follows. In the next section, the experimental setup is presented. In Section 3, the proposed control scheme including an inverse hysteresis compensator, an integral resonant controller, a feedback tracking controller and a feedforward input is developed. After that, comparative experiments and evaluations are performed in Section 4, followed by the conclusion in Section 5.

2. Experimental setup

A flexure-guided nanopositioning stage is used in this paper to implement and test the proposed control scheme. The stage is actuated by a preloaded piezoceramic stack actuator (PSA) from Piezomechanik in Germany. A power amplifier with a gain of 15 is used to drive the PSA. A high-resolution strain gauge sensor (SGS) integrated into the PSA is adopted to measure the real-time position. A signal conditioner is used to convert the measured position to analog voltage in the range of 0–10 V. A dSPACE DS1103 board equipped with the 16-bit DAC and 16-bit ADC is utilized to output the excitation for the power amplifier and capture the real-time displacement information from the signal conditioner. As an illustration, the experimental platform is shown in Fig. 1a.

For modeling and control purpose, the PSA-actuated nanopositioning system is treated as a signal-input-signal-output system. The input is the voltage v applied to the piezo amplifier and the output is the corresponding displacement y from the SGS. The block diagram of the entire experimental setup is shown in Fig. 1b. In the following development, the proposed control scheme will be addressed in detail.

3. Controller design

The control objective in high-bandwidth nanopositioning is to not only minimize the tracking error but also maximize the tracking speed of the PSA. As the actuator is inherently nonlinear (i.e. the hysteresis nonlinearity) and lightly damped, it requires the multi-algorithm fusion control strategy in the control loop. In this paper, an inverse hysteresis compensator is firstly adopted to cancel the hysteresis nonlinearity. Then, an integral resonant controller is utilized to damp the hysteresis compensated system's first resonant mode. Finally, an integral controller and a feedforward input are implemented to achieve high-bandwidth nanopositioning of the PSA.

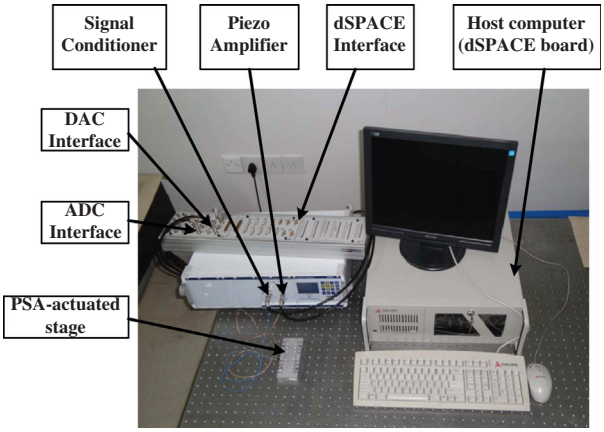

(a) Experimental platform

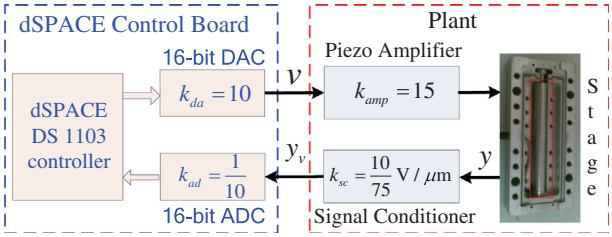

(b) Block diagram

Fig. 1. The experimental setup.

3.1. Hysteresis compensator

In this section, we characterize and compensate for the hysteresis nonlinearity of the PSA. The compensation is necessary in order to linearize the system and therefore to make easy the synthesis of a linear integral resonant controller for vibration damping in the following development.

The first step in constructing the inverse hysteresis compensator is to characterize the hysteresis nonlinearity in the PSA with an effective hysteresis model. The hysteresis of the PSA is an inherent multi-valued nonlinearity with the asymmetric characteristic, which can be observed in the relationship between the applied voltage and corresponding displacement of the PSA shown in Fig. 2. To describe this asymmetric hysteresis, the modified Prandtl-Ishlinskii (MPI) model [29] defined in terms of weighted play operators and a polynomial input function is utilized in this work

$$y(t) = P_g[v](t) = g(v(t)) + \int_0^R p(r)F_r[v](t)dr \tag{1}$$

where $v(t)$ is the input, $y(t)$ is the output, $g(v(t)) = a_1 v^3(t) + a_2 v(t)$ is a polynomial input function with constant a_1 and a_2, $p(r)$ is a density function that is generally calculated from the experimental data, and $F_r[v](t)$ is a one-side play operator expressed as

$$\begin{aligned} F_r[v](0) &= f_r(v(0), 0) \\ F_r[v](t) &= f_r(v(t), F_r[v](t_i)) \end{aligned} \tag{2}$$

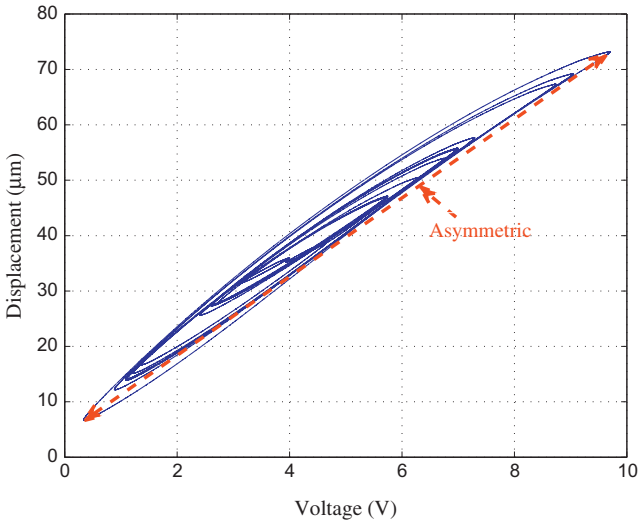

Fig. 2. The hysteresis nonlinearity of the PSA.

for $t_i < t \leqslant t_{i+1}, 0 \leqslant i \leqslant N-1$ with

$$f_r(v,w) = \max(v-r, \min(v,w)) \tag{3}$$

where $0 = t_0 < t_1 < \cdots < t_N = t_E$ is a partition of $[0, t_E]$, such that the function $v(t)$ is monotone on each of the subintervals $[t_i, t_{i+1}]$. The argument of the operator $F_r[v](t)$ is written in square brackets to indicate the functional dependence, since it maps a function to another function. The reader may refer to [29] for detailed descriptions and discussions of the MPI model.

To compensate for a hysteresis nonlinearity that has been modeled with a hysteresis model Γ, the common idea is to construct the inverse hysteresis model Γ^{-1}, which is put in series with the real hysteretic system as shown in Fig. 3. In order to conveniently implement the real-time inverse hysteresis compensator, the definition of MPI model given in (1) can be approximated in the discrete form with a finite number of the play operators as follows

$$y_g(t) = P_g[v](t) = a_1 v^3(t) + a_2 v(t) + \sum_{i=1}^{n} b(r_i) F_{r_i}[v](t) \tag{4}$$

where n is the number of the adopted play operators for modeling, and $b(r_i)$ is the weighted constant for the threshold r_i. In this work, to describe the asymmetric hysteresis of the tested PSA, the value of n is chosen as 10, and the threshold values r_i in the MPI model (4) are chosen as

$$r_i = \frac{i-1}{n} ||v(t)||_\infty, \quad i = 1, 2, \ldots, n \tag{5}$$

with $||v(t)||_\infty = 1$ in the normalized case. The weighted parameters $b(r_i)$, and coefficients a_1 and a_2 of polynomial input function in (4) are identified by the particle swarm optimization algorithm [29], which are listed in Table 1. As shown in Fig. 4, the hysteresis loops generated by the identified MPI model are also compared with the experimental results, which clearly verifies the effectiveness of the model.

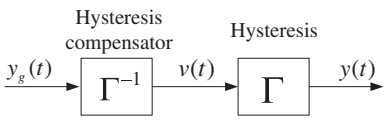

Fig. 3. Block representation for inverse hysteresis compensation.

Table 1
Identified parameters of the MPI model.

Number	r_i	b_i	a_i
1	0	0.2313	−0.1569
2	0.1	0.3059	0.4603
3	0.2	0.0155	
4	0.3	0.0752	
5	0.4	0.0683	
6	0.5	0.0252	
7	0.6	0.0035	
8	0.7	0.0094	
9	0.8	0.0264	
10	0.9	0.0032	

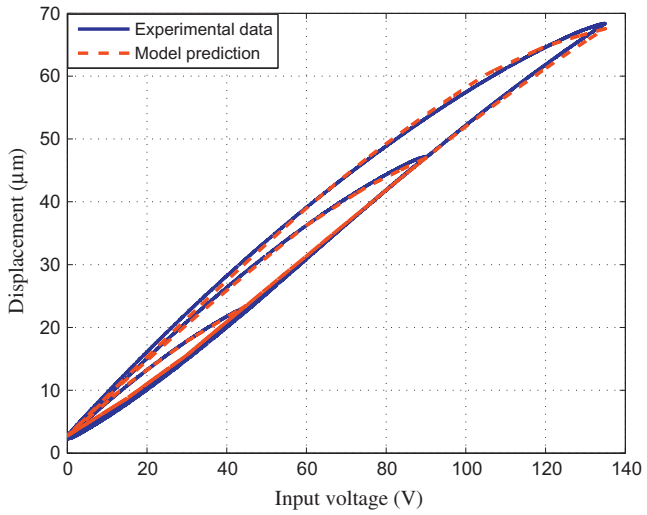

Fig. 4. Comparison of the hysteresis loops generated by the PSA and the identified MPI model.

On the basis of the inverse model of the classical Prandtl-Ishlinskii (CPI) model [9] and inspired by the work in [30], the MPI model (4) is re-expressed as the following superposition [29]

$$y_g(t) = P_g[v](t) = P_c[v](t) + P[v](t) \tag{6}$$

where $P_c[v](t) = a_1 v^3(t)$ is a new model component, and $P[v](t) = a_2 v(t) + \sum_{i=1}^{n} b(r_i) F_{r_i}[v](t)$ is by nature the CPI model [9].

The synthesis of efficient real-time control algorithms for the compensation of the asymmetric hysteresis nonlinearity represented by the MPI model is based on the implicit operator equation

$$v(t) = P^{-1}[w](t) \tag{7}$$

for the inverse compensator

$$v(t) = P_g^{-1}[y_g](t) \tag{8}$$

where $w = y_g - P_c[v]$, and P^{-1} is the inverse of the CPI model expressed as

$$P^{-1}[w](t) = \hat{a}_2 w(t) + \sum_{j=1}^{n} \hat{b}_j F_{\hat{r}_j}[w](t) \tag{9}$$

with

$$\begin{aligned} \hat{r}_j &= a_2 r_j + \sum_{i=1}^{j-1} b_i (r_j - r_i) \\ \hat{a}_2 &= \frac{1}{a_2} \\ \hat{b}_j &= -\frac{b_j}{\left(a_2 + \sum_{i=1}^{j-1} b_i\right)\left(a_2 + \sum_{i=1}^{j} b_i\right)} \end{aligned} \tag{10}$$

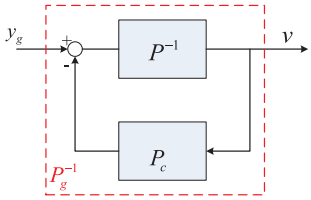

Fig. 5. Signal flow chart of the inverse compensator P_g^{-1}.

By this way, the analytical inverse hysteresis model of the MPI model can be obtained. As an illustration, Fig. 5 shows the signal flow chart of the inverse compensator P_g^{-1} for the MPI model. The MPI inverse compensator has been implemented for hysteresis compensation. Fig. 6 shows the experimental results with and without the inverse compensator and demonstrates that the hysteresis has been reduced to 3.3% instead of about $13.6\%(=\frac{h}{H}\times 100\%)$ without the inverse compensation. It can be seen that the hysteresis nonlinearity is greatly mitigated with the inverse hysteresis compensator and the resulted relationship between the desired position and the actual position is almost linear and symmetric. In the following development, the integral resonant controller can be designed for the hysteresis compensated system to attenuate its vibration effect.

3.2. Damping controller

In this section, the integral resonant control (IRC) strategy is applied as a means for damping the dynamic system with the hysteresis compensation. For the purpose of IRC design and analysis, a model of the linear dynamic system is required [25,28]. In Section 3.1, the inverse hysteresis compensator is introduced to mitigate the hysteresis linearity, which makes it possible to identify the linearized dynamic system (i.e. the PSA-actuated stage with the inverse hysteresis compensation) for the IRC design.

As reported in our previous work [4], the PSA-actuated stage can be modeled as a third-order linear dynamic model preceded by an input hysteresis nonlinearity. In Section 3.1, the hysteresis nonlinearity has been compensated by the IHC. Therefore, the dynamic model of the hysteresis compensated system can be represented as a third-order structure. To identify the model, a bandlimited white noise signal is used to excite the hysteresis compensated system. The dSPACE control system is utilized to simultaneously capture the excitation voltage and the corresponding measured displacement. Then, the system identification toolbox of MATLAB can be adopted to obtain the identified dynamic model represented as

$$G(s)=\frac{Y(s)}{Y_g(s)}=\frac{470.4068(s^2+4.067e004s+5.882e008)}{(s+2726)(s^2+4030s+1.067e008)}. \quad (11)$$

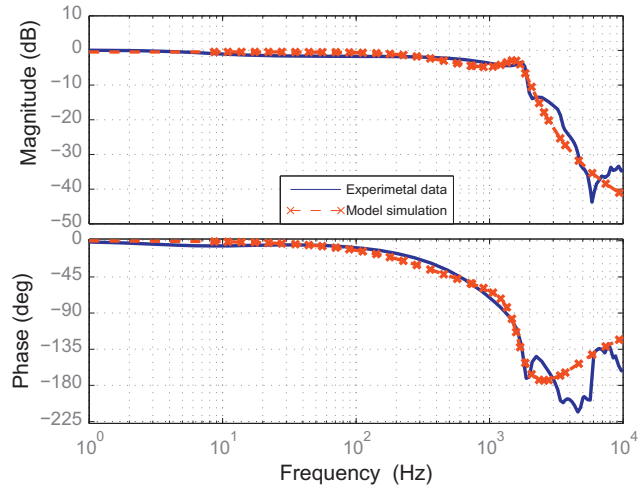

Fig. 7. Comparison of frequency responses of experimental results and model simulation results.

Fig. 7 shows the comparison of frequency responses of experimental results and model simulation results to demonstrate the effectiveness of the identified model. It can be seen that the identified model captures the dynamics of the system with sufficient accuracy.

The principle of the IRC strategy [25,28] is represented as the block diagram in Fig. 8a. It consists of a linear collocated dynamic system G_2, a constant artificial feed-through term D_f with $D_f<0$, and an integral controller C. The objective of the IRC strategy is to design the artificial feed-through term D_f and the integral controller C such that the resonant modes of the system G_2 are damped. For simplicity, an equivalent block diagram of the IRC strategy [25] is also shown in Fig. 8b. It should be mentioned that

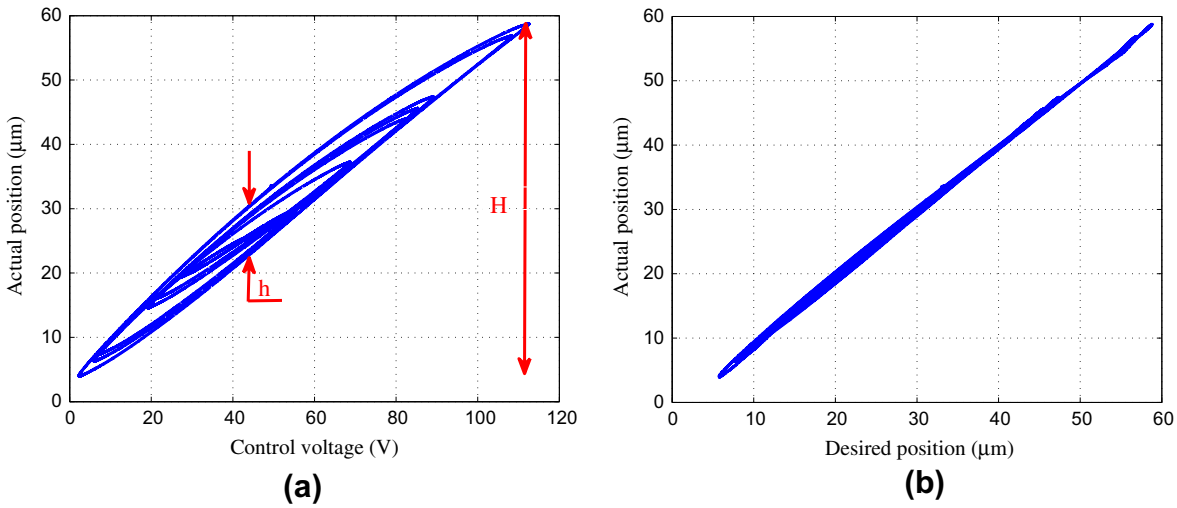

Fig. 6. (a) Curves showing the hysteresis of the PSA in open loop control. (b) Curves showing the measured position versus the desired input using the inverse hysteresis compensator. Experimental results with and without the inverse hysteresis compensator.

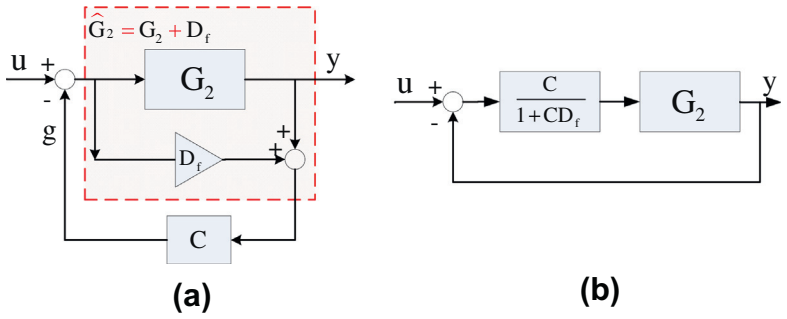

Fig. 8. (a) Schematic diagram of the IRC strategy. (b) Equivalent schematic diagram of the IRC strategy.

in the IRC strategy, the dynamic system G_2 is generally a two-order transfer function with the form of $\frac{K(s^2+2\xi_1\omega_1 s+\omega_1^2)}{s^2+2\xi_2\omega_2 s+\omega_2^2}$ [25]. By applying the IRC strategy for the system (11) in this work, the model (11) should be re-expressed as

$$G(s) = G_1(s) \times G_2(s). \tag{12}$$

with

$$\begin{cases} G_1(s) = \frac{2726}{s+2726} \\ G_2(s) = \frac{0.1726s^2+7020s+1.015e008}{s^2+4030s+1.067e008}. \end{cases} \tag{13}$$

The first step in applying the IRC strategy is to determine the artificial feed-through term D_f. As shown in Fig. 8a, by introducing the feed-through term D_f, an augmented system $\widehat{G}_2 = G_2 + D_f$ is formed. It can be seen that the augmented system $\widehat{G}_2$ and the original system G_2 have the same poles. By selecting a sufficient D_f, a pair of zeros below the first resonant mode is introduced to guarantee zero-pole interlacing for higher frequency modes [25,28].

For the model G_2 described in (13), using the root-locus technique [25], a feed-through term of $D_f = -1.8$ is chosen to introduce a pair of zeros below the first resonance mode. The frequency responses of the open-loop system G_2 and the augmented system $G_2 + D_f$, where $D_f = -1.8$, are plotted in Fig. 9. It can be seen that the feed-through term D_f introduces a pair of complex zeros at the frequency of 1.19 kHz to provide a phase lead. It should be noted that due to the negative sign in $\widehat{G}_2$ additional -180° makes the phase response of the modified transfer function lie between -180° and 0° as shown in Fig. 9.

With the modified transfer function $\widehat{G}_2$, the augmented transfer function G_m for (12) is obtained as $G_m = G_1 \times \widehat{G}_2$. Fig. 9b also shows the frequency response for the augmented transfer function G_m. It is observed that the phase of G_m is bounded between -270° and -90° due to the introduction of the feed-through term D_f. Therefore, a simple negative integral

$$C(s) = \frac{-k}{s}, \quad \text{with } k > 0 \tag{14}$$

can be applied to provide a 90° phase lead. To evaluate the stability of such a controller, the loop gain of CG_m is examined. Thus, the phase of CG_m is equal to the phase of G_m plus 90°. The resulting phase response will be within -180° and 0°, which produces excellent phase margin and infinite gain margin. Using the root-locus technique [25,28], the controller gain k is chosen as 754 to maximize damping. In such a case, Fig. 10 shows the frequency response of the open-loop transfer function for verification.

Remark: It should be noted that the IRC is designed based on the linear control theory using a transfer function method, which cannot be directly applied to handle the non-smooth hysteresis nonlinearity of the PSA-actuated system. In this work, the IHC is introduced in advance to remedy the hysteresis nonlinearity. As a result, the PSA-actuated system with the IHC is by nature treated as a linear dynamic system, which makes it possible to develop the IRC. Therefore, the IHC part developed in Section 3.1 is a necessary control unit for the IRC design in our proposed control scheme.

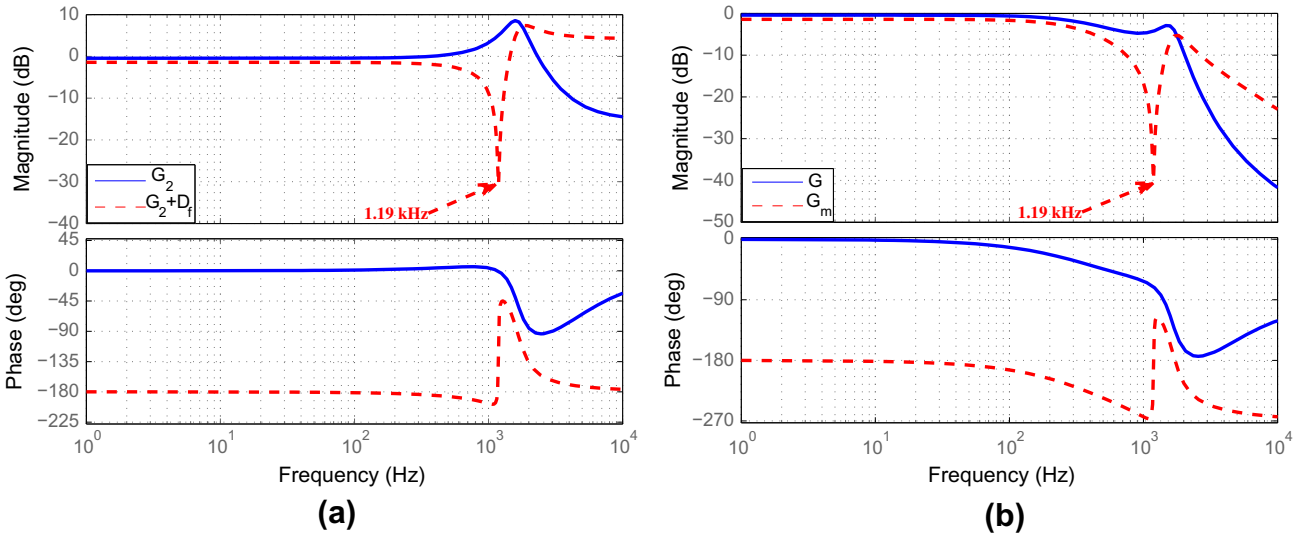

Fig. 9. (a) G_2 and $G_2 + D_f$. (b) G and G_m Frequency responses to describe the effect of the feed-through term D_f on the transfer functions G_2 and G.

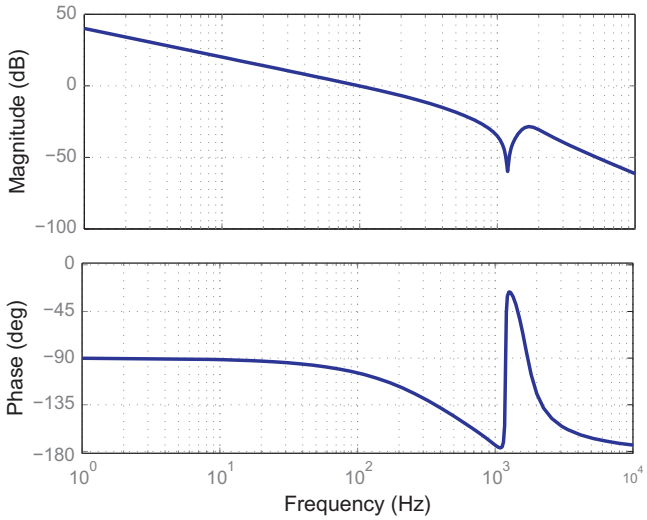

Fig. 10. Frequency responses of the open-loop transfer function CG_m with $k = 754$.

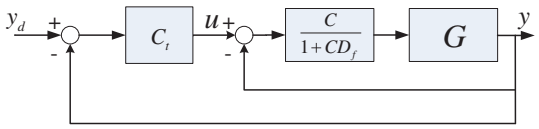

Fig. 11. Block of the tracking control system with the IRC controller and tracking controller.

3.3. Tracking controller

The foremost control objective in nanopositioning is to minimize tracking errors between the desired position y_d and the actual position y. In the aforementioned sections, we have addressed related compensation methods for the hysteresis and vibration effects. In this section, a secondary feedback tracking controller C_t is designed to compensate for disturbances and modeling uncertainties as shown in Fig. 11.

As addressed in Section 3.2, the IRC strategy has been utilized to overcome the challenge of the low gain margin problem [7,31] in the PSA. It thus enables to design a high-gain tracking controller for the system after the IRC compensation. Due to the inverting behavior of the IRC loop [25], a proportional-integral controller C_t with a negative sign is developed in this work, whose transfer function is expressed as

$$C_t(s) = -\frac{k_p s + k_i}{s} \tag{15}$$

where $k_p > 0$ is the proportional gain and $k_i > 0$ is the integral gain.

Therefore, the transfer function of the closed-loop system is expressed as

$$\frac{Y(s)}{Y_d(s)} = \frac{C_t(s)C_1(s)G(s)}{1 + C_1(s)(1 + C_t(s))G(s)} \tag{16}$$

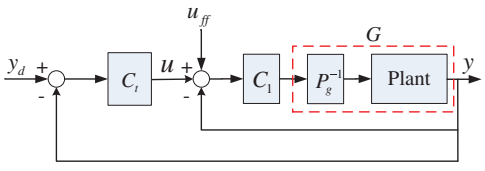

Fig. 12. Block diagram of the proposed control scheme with the inverse hysteresis compensator P_g^{-1}, the IRC controller C_1, the tracking controller C_t and the feedforward input u_{ff}.

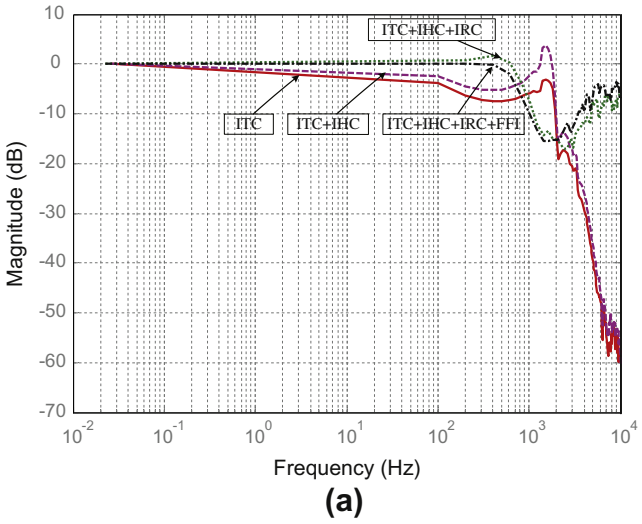

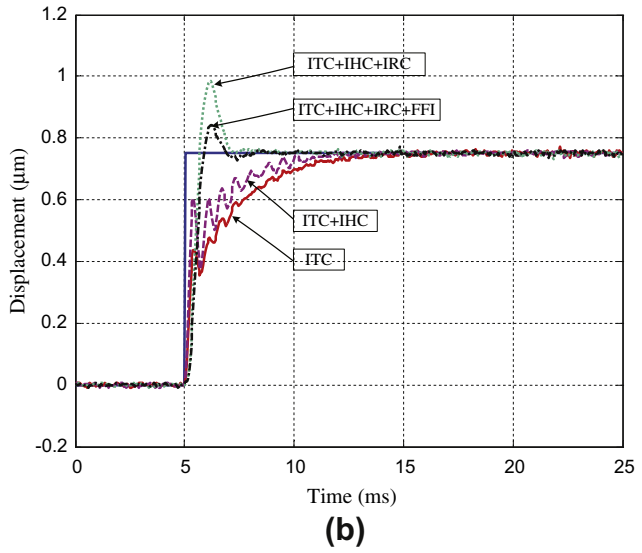

Fig. 13. Control performance comparison of the four developed control strategies. (a) Frequency responses. (b) Step responses.

Table 2
Control parameters and performances of the four kinds of controllers.

Controller	ITC	ITC + IHC	ITC + IHC + IRC	ITC + IHC + IRC + FFI
C_t	$\frac{s+1000}{s}$	$\frac{s+1000}{s}$	$-\frac{4s+3500}{s}$	$-\frac{4s+3500}{s}$
P_g^{-1}	0	Eq. (8)	Eq. (8)	Eq. (8)
C_1	0	0	$-\frac{754}{s+1357}$	$-\frac{754}{s+1357}$
u_{ff}	0	0	0	0.8922
Bandwidth (Hz)	22	118	779	657
Setting time (ms)	9	7	4	3
Vibration	Large	Large	Small	Small
Overshoot	Small	Small	Large	Small

with

$$C_1(s) = \frac{C(s)}{1 + C(s)D_f}. \tag{17}$$

3.4. Feedforward controller

Feedforward control is an effective method to improve the tracking bandwidth of a closed-loop system by bypassing the

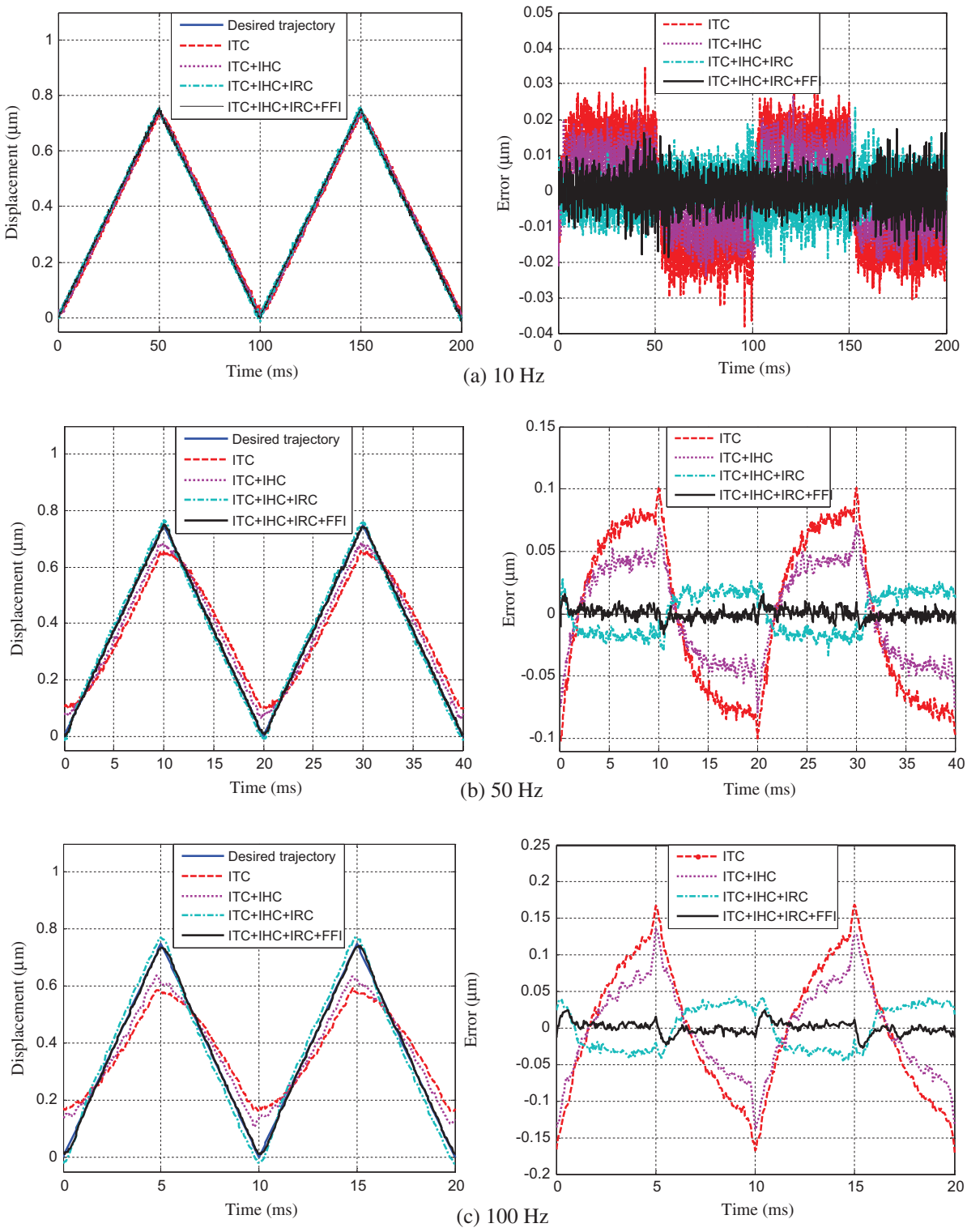

Fig. 14. Comparison of the tracking performances of the different controllers for triangular trajectories under various input frequencies.

tracking controller or inverting dynamics [18,25,32,33]. Similar to the reported work in [25], the inverse dc gain of the system is simply used to provide the performance improvement in this application and we will verify this further in the following experiments.

In this work, the feedforward input is denoted as u_{ff}, which is generated by the reference input and the inverse dc gain of the damped system as follows

$$u_{ff} = y_d\left(\frac{C_1(s)G(s)}{1+C_1(s)G(s)}\bigg|_{s=0}\right)^{-1}. \tag{18}$$

Therefore, the block diagram of the proposed control scheme with the inverse hysteresis compensator P_g^{-1}, the IRC controller C_1, the tracking controller C_t and the feedforward input u_{ff} is schematically shown in Fig. 12.

4. Experimental implementation

In this section, the proposed control scheme is implemented on the PSA-actuated stage described in Section 2. For ease of comparison, four controllers are designed: (1) the integral tracking controller (ITC); (2) the integral tracking controller with the inverse hysteresis compensator (ITC + IHC); (3) the integral tracking controller with the inverse hysteresis compensator and the IRC damping (ITC + IHC + IRC); and (4) the integral tracking controller with the inverse hysteresis compensator, the IRC damping and the feedforward input (ITC + IHC + IRC + FFI).

(1) ITC: It is well known that higher control gains for k_p and k_i commonly contribute to smaller tracking errors and faster trajectory convergence. However, doing so may compromise the stability of the system. Therefore, the values of k_p and k_i cannot be arbitrarily set, and a tradeoff between stability and performance need to be experimentally established when tuning the parameter values. In this work, the ITC was designed to maximize tracking bandwidth. The maximum gain was restricted to $k_p = 1$ and $k_i = 1000$ by the gain-margin of only 2.9 dB. Fig. 13a shows the experimental frequency response of the system with the ITC. It can be seen that the control bandwidth (i.e. -3 dB bandwidth) of the ITC is 22 Hz. Fig. 13b shows the step response of the system with the ITC. We observe that the output exhibits oscillations and converges slowly with a steady state error of roughly 15 nm after about 9 ms.

(2) ITC + IHC: By adding an asymmetric inverse hysteresis compensator to the ITC as addressed in Section 3.1, the bandwidth can be extended to 118 Hz at the expense of gain-margin as shown in Fig. 13a. From the step response shown in Fig. 13b, the output converges more quickly than in the case of the ITC, while it exhibits more undesirable oscillations due to the lightly damped resonance mode.

(3) ITC + IHC + IRC: Following the procedure in Section 3.2, the IRC damping controller was further designed for the system to tackle the low gain margin problem of the resonant modes in the PSA-actuated system. It should be mentioned that it is the IRC that make the larger control gains of k_p and k_i possible, which is the motivation of this work to develop the IRC for high-bandwidth control of the PSA. Thereafter, a high-gain ITC with $k_p = 4$ and $k_i = 3500$ was developed while maintaining the gain-margin of 13 dB. In this case, as shown in Fig. 13a, the control bandwidth is extended to 779 Hz. However, some of this bandwidth is uncontrolled. The faster response can also be demonstrated by the step response shown in Fig. 13b, where a large overshoot is observed.

(4) ITC + IHC + IRC + FFI: To further improve the control performance, the FFI as addressed in Section 3.4 was finally introduced in the developed controller. As shown in Fig. 13, the effect of the improved bandwidth is demonstrated by both the frequency response and step response. Compared with the results of the ITC + IHC + IRC controller, the overshoot is significantly reduced, while a higher control bandwidth is possessed. In summary, Table 2 lists the control parameters and performances of the four kinds of controllers for comparison.

As a last example to evaluate the tracking performance, Fig. 14 shows the experimental results of the closed-loop system with different controllers for triangular trajectories under various input frequencies. In addition, the RMS tracking errors are compared in Table 3. From the figure and table, it can be demonstrated that the high-speed and high-precision performances of the proposed ITC + IHC + IRC + FFI controller is significantly better than the others.

Table 3
RMS tracking errors for triangular trajectories under various input frequencies.

Controller	10 Hz	50 Hz	100 Hz
ITC	16.0 nm	63.1 nm	90.4 nm
ITC + IHC	9.6 nm	38.4 nm	62.4 nm
ITC + IHC + IRC	5.5 nm	16.8 nm	29.7 nm
ITC + IHC + IRC + FFI	4.0 nm	4.6 nm	8.6 nm

5. Conclusion

In this paper, we present a novel control scheme for high-precision and high-bandwidth control of the PSA. The control scheme first deals with the asymmetric hysteresis nonlinearity by an inverse hysteresis compensator. As a result, the linear IRC strategy can be applied as a means for damping the resonant modes of the dynamic system with the inverse hysteresis compensation. Finally, the tracking controller and the feedforward input are designed to achieve the fast nanopositioning of the PSA. We have demonstrated the effectiveness and efficiency of the proposed method when applied to a PSA-actuated positioning stage. The comparative experimental results confirm that the proposed controller successfully increases the closed-loop tracking bandwidth of the traditional integral tracking controller from 22 Hz to 657 Hz.

Acknowledgements

This work was supported by the National Natural Science Foundation of China under Grant No. 91023047, and Shanghai Postdoctoral Scientific Program under Grant No. 13R21414000. The Science and Technology Commission of Shanghai Municipality under Grant 11520701500, and China Postdoctoral Science Foundation under Grant 2013M530193.

References

[1] Devasia S, Eleftheriou E, Moheimani SOR. A survey of control issues in nanopositioning. IEEE Transactions on Control Systems Technology 2007;15(5):802–23.
[2] Salapaka SM, Salapaka MV. Scanning probe microscopy. IEEE Control Systems Maganize 2008;28(2):65–83.
[3] Park G, Bement MT, Hartman DA, Smith RE, Farrar CR. The use of active materials for machining processes: a review. International Journal of Machine Tools and Manufacture 2007;47(15):2189–206.
[4] Gu GY, Zhu LM, Su CY, Ding H. Motion control of piezoelectric positioning stages: modeling, controller design and experimental evaluation. IEEE/ASME Transactions on Mechatronics 2012. http://dx.doi.org/10.1109/TMECH.2012.2203315.
[5] Goldfarb M, Celanovic N. Modeling piezoelectric stack actuators for control of micromanipulation. IEEE Control Systems Magazine 1997;17(3):69–79.
[6] Ando T, Uchihashi T, Fukuma T. High-speed atomic force microscopy for nano-visualization of dynamic biomolecular processes. Progress in Surface Science 2008;83(7–9):337–437.
[7] Leang KK, Devasia S. Feedback-linearized inverse feedforward for creep hysteresis and vibration compensation in AFM piezoactuators. IEEE Transactions on Control Systems Technology 2007;15(5):927–35.
[8] Ge P, Jouaneh M. Tracking control of a piezoceramic actuator. IEEE Transactions on Control Systems Technology 1996;4(3):209–16.
[9] Krejci P, Kuhnen K. Inverse control of systems with hysteresis and creep. IEE Proceedings of Control Theory and Applications 2001;148(3):185–92.
[10] Davino D, Natale C, Pirozzi S, Visone C. A fast compensation algorithm for real-time control of magnetostrictive actuators. Journal of Magnetism and Magnetic Materials 2005;290:1351–4.
[11] Iyer RV, Tan X. Control of hysteretic systems through inverse compensation. IEEE Controls Systems Magazine 2009;29(1):83–99.
[12] M. Ruderman, T. Bertram, Discrete dynamic Preisach model for robust inverse control of hysteresis systems, in: 49th IEEE Conference on Decision and Control, 2010, pp. 3463–3468.
[13] Xu Q, Wong PK. Hysteresis modeling and compensation of a piezostage using least squares support vector machines. Mechatronics 2011;21(7):1239–51.
[14] Chen X, Hisayam T. Adaptive sliding-mode position control for piezo-actuated stage. IEEE Transactions on Industrial Electronics 2008;55(11):3927–34.
[15] Sebastian A, Salapaka S. Design methodologies for robust nano-positioning. IEEE Transactions on Control Systems Technology 2005;13(6):868–76.
[16] Liaw HC, Shirinzadeh B, Smith J. Enhanced sliding mode motion tracking control of piezoelectric actuators. Sensors and Actuators A: Physical 2007;138(1):194–202.
[17] Fleming AJ, Leang KK. Charge drives for scanning probe microscope positioning stages. Ultramicroscopy 2008;108(12):1551–7.

[18] Clayton GM, Tien S, Leang KK, Zou Q, Devasia S. A review of feedforward control approaches in nanopositioning for high-speed SPM. Journal of Dynamic Systems, Measurement and Control 2009;131(6):1–19. 061101.
[19] Lee C, Salapaka S. Robust broadband nanopositioning: fundamental, trade-offs analysis, and design in a two-degree-of-freedom control framework. Nanotechnology 2009;20(3):035501.
[20] Schitter G, Thurner PJ, Hansma PK. Design and input-shaping control of a novel scanner for high-speed atomic force microscopy. Mechatronics 2008;18(5–6):282–8.
[21] Rakotondrabe M, Clevy C, Lutz P. Complete open loop control of hysteretic, creeped and oscillating piezoelectric cantilevers. IEEE Transactions on Automation Science and Engineering 2010;7(3):440–50.
[22] Vorbringer-Dorozhovets N, Hausotte T, Manske E, Shen JC, Jager G. Novel control scheme for a high-speed meteorological scanning probe microscope. Measurement Science and Technology 2011;22(9):094012.
[23] Croft D, Shed G, Devasia S. creep, hysteresis and vibration compensation for piezoactuators: atomic force microscopy application. ASME Journal of Dynamic Systems Measurement and Control 2001;123(1):35–43.
[24] Al-Mamun A, Keikha E, Bhatia CS, Lee TH. Integral resonant control for suppression of resonance of piezoelectric micro-actuator used in precision servomechanism. Mechatronics 2013;23(1):1–9.
[25] Fleming AJ, Aphale S, Moheimani SOR. A new method for robust damping and tracking control of scanning probe microscope positioning stages. IEEE Transactions on Nanotechnology 2010;9(4):438–48.
[26] Song G, Schmidt SP, Agrawal BN. Experimental robustness study of positive position feedback control for active vibration suppression. Journal of Guidance Control and Dynamics 2002;25(1):179–82.
[27] Pota H, Moheimani SOR, Smith M. Resonant controllers for smart structures. Smart Materials and Structures 2002;11(5):1–8.
[28] Aphale S, Fleming AJ, Moheimani SOR. Integral resonant control of collocated smart structures. Smart Materials and Structures 2007;16(2):439–46.
[29] Gu GY, Zhu LM, Su CY. Modeling and compensation of asymmetric hysteresis nonlinearity for piezoceramic actuators with a modified Prandtl–Ishlinskii model. IEEE Transactions on Industrial Electronics 2013. http://dx.doi.org/10.1109/TIE.2013.2257153.
[30] Kuhnen K, Krejci P. Compensation of complex hysteresis and creep effects in piezoelectrically actuated systems – a new Preisach modeling approach. IEEE Transactions on Automatic Control 2009;54(3):537–50.
[31] Salapaka S, Sebastian A, Cleveland JP, Salapaka MV. High bandwidth nano-positioner: a robust control approach. Review of Scientific Instruments 2002;793(9):3232–41.
[32] Yi L, Tomizuka M. Two-degree-of-freedom control with robust feedback control for hard disk servo systems. IEEE/ASME Transactions on Mechatronics 1999;4(1):175–81.
[33] Butterworth JA, Pao LY, Abramovitch DY. A comparison of control architectures for atomic force microscopes. Asian Journal of Control 2009;11(2):175–81.